Query Details

Back to Main Page

1. Please check the edit made in the article title.
2. Please provide part figure label a definition for Fig. 7.
3. Please provide volume no and page range for Reference [5].
4. Please provide page range for References [6,7, 9, 10].
5. Reference [43] is given in list but not cited in text. Please cite in text or delete from list.
6. Please provide complete details of Reference [52].

Inkjet-printed frequency-selective surfaces based on carbon nanotubes for ultra-wideband thin microwave absorbers

R. Jaiswar, [1]

F. Mederos-Henry, [2]

V. Dupont, [3]

S. Hermans, [2]

J. -P. Raskin, [1]

I. Huynen, [1]✉

Email isabelle.huynen@uclouvain.be

[1] ICTEAM Institute, ELEN Division, Université catholique de Louvain (UCLouvain), 3 place du Levant, 1348 Louvain-la-Neuve, Belgium

[2] IMCN Institute, MOST Division, UCLouvain, 1 place Lavoisier, 1348 Louvain-la-Neuve, Belgium

[3] Belgian Ceramic Research Centre, 4 avenue Gouverneur, Cornez, 7000 Mons, Belgium

Received: 24 October 2019 / Accepted: 11 December 2019

Abstract

A microwave absorber combining frequency-selective surfaces (FSSs) and dielectric layers is presented. FSSs are printed on dielectric layers using a resistive ink made of a suspension of carbon nanotubes. The absorber exhibits a fractional bandwidth of 137%, corresponding to reflectivity lower than -15 dB and absorption higher than 90% from 7.30 till 41.95 GHz, meaning a 34 GHz bandwidth, for a thickness of only 0.13 λ. This performance is obtained by tuning the number of printed layers, which fixes FSS resistivities, hence the absorption bandwidth. An electrical equivalent circuit is proposed to explain the absorption mechanism. Excellent agreement is observed between the designed and measured low reflectivity and high absorption. The absorber stands out in term of bandwidth and compacity as compared to the state of the art.

AQ1

1. Introduction

Carbon-based nanostructures such as carbon nanotubes and graphene have been widely used for applications in electronics, in particular related to (bio)sensors [1, 2, 3, 4, 5, 6, 7], fuel cell electrodes, memristors [8] and supercapacitors [9, 10, 11] as well as mechanical reinforcers [12]. In all these applications, the interactions between carbon structures and signals are exploited to create novel devices displaying enhanced performances. Another kind of interaction has been recently exploited to counteract detrimental effects of electromagnetic waves. Indeed, extensive use of wireless electronics and telecommunication devices in our daily life is causing increasing electromagnetic (EM) pollution and undesirable radiative effects on electronic equipment as well as, potentially, on human health.

Engineered EM metamaterial structures have attracted a tremendous research interest for both commercial and defense applications owing to their peculiar electromagnetic properties such as negative refractive index, near-zero permittivity and permeability and sub-wavelength imaging. In the microwave band, extensive research has been conducted to develop metamaterial inspired filters, polarizers, sensors, cloaking devices, shielding devices, microwave absorbers and so on [13, 14]. In the last decade, metamaterial-based microwave absorbers have been widely researched due to their simplicity in planar design, ease of fabrication, low-cost and high-volume production [15, 16].

In the past, classical Salisbury screens and similar structures were widely reported for microwave absorption; however, their narrow bandwidth and large thickness have limited their application [17, 18]. Jaumann absorbers were developed using a number of homogenous resistive sheets on dielectric layers that are stacked together to achieve broadband operation at the cost of high thickness [19, 20]. In the recent past, researchers have proposed the circuital analysis approach for Jaumann absorber where frequency-selective surface (FSS) is employed instead of the homogenous resistive sheets to facilitate the broadband absorption at lowered thicknesses [21, 22]. FSS can be designed to achieve filtering effects such as low-pass, band-stop, and narrow peak filters through the controlled variation in surface admittance via geometric parameters of FSS. Thin FSS-based absorbers loaded with lumped elements to achieve improved absorption bandwidth were also reported [23, 24]. Metallic FSS makes the structure more complex to manufacture and costly. An excellent alternative to this approach consists in printing the FSS using resistive ink with proper surface resistance and using some design guidelines to develop the microwave absorber [25, 26, 27].

On other hand, Rozanov [28] proposed the ultimate theoretical limit for the absorber thickness, which can be physically realized for the absorber’s operating in a specific frequency band. The Rozanov’s theory is applicable on homogeneous multilayers only, but it is still a convincing landmark to assess the efficiency of 3D-patterned multilayers [28]. Generally, absorption of electromagnetic waves is understood through lowered reflection at input of composite and/or dissipation of electromagnetic energy inside the composite medium [15, 16]. As reported in [29, 30, 31, 32, 33], an efficient way to do that consists of including magnetic particles combined with conductive fillers in the structure of an absorber in order to favor absorption while lowering reflection at its input.

Low conductivity or resistively printed FSS on dielectric substrate also enables to modify and reduce the input impedance of the absorber not only by the geometry of FSS but also through surface resistance (R_s) of the printed layer [34, 35, 36, 37]. Printed electronics provides another set of advantages compared to the conventional lithography technology by facilitating low-cost high production, ease of fabrication, reduced material waste and flexibility [38, 39]. For conductive ink material used to print FSSs, conventional metals are available on the market such as silver (Ag), gold (Au) and copper (Cu) [40, 41]. Silver and gold are too expensive for making conductive ink, and on other hand, copper suffers from oxidation issues. An alternative uses carbonaceous material such as carbon nanotubes (CNTs) and graphene nanoplatelets (GNPs) which possess excellent electrical and mechanical properties [42, 43], thermal and chemical stability, high aspect ratio, and are cost-effective. Thus, they are perfect candidates as conductive material to be utilized for an ink material [44, 45, 46]. Primary requirements of these microwave absorbers are manifold: wide operational bandwidth, lowered reflectivity $(< -10\text{\,dB})$, lower absorber thickness, along with ease of fabrication and low-cost fast production.

In this paper, we present a thin ultra-wideband microwave absorber (UWMA) based on inkjet-printed frequency-selective surfaces (FSSs) on polycarbonate films supported on low-dielectric spacers. The required optimized surface impedance is achieved through homemade carbon nanotube (1 wt%) water-based ink (CNT-ink) developed for inkjet printing. An equivalent circuit is proposed to explain the operation of the UWMA and assist in its design. The proposed microwave absorber achieved excellent agreement between measured and simulated results showing -15 dB reflectivity over a 34 GHz bandwidth, between 7 and 41 GHz, which corresponds to a huge 137% fractional absorption bandwidth (FBW) for an absorber thickness of only 5.1 mm. These performances are successfully compared with the state of the art and the Rozanov limit. The stability of the UWMA operation with respect to incidence of signal was also verified.

2. Materials and methods

2.1. Carbon nanotubes ink : preparation and printing

Materials considered are Multiwall carbon nanotubes (MWCNT, Nanocyl 7000 from Nanocyl SA) and dispersants Triton X100 and TEGO®Dispers 765 W. A simple sonication approach was employed to prepare the ink. Triton X100 was firstly incorporated in distilled water containing MWCNT to decrease the surface tension of the distilled water and maintain MWCNT in suspension. Next, sonication was carried out with Bioblock Scientific Vibracell 75041 during 6 min (10 s ON; 10 s OFF). After this, the solution became a gel, and another dispersant, Dispers 765 W, was incorporated in order to ensure a very fluid suspension. Finally, the MWCNT suspension was centrifuged using Heraeus Sepatech 2520 to remove some impurities or possible remaining MWCNT aggregates which could clog nozzles of the print heads. The resulting suspension became very stable in time and very opaque without clarification. The main characteristics of the elaborated MWCNT's ink are viscosity, surface tension and density, which are listed in Table 1. These values were selected in order to ensure an uniform printing of the layers and avoid clogging of inkjet cartridge nozzles.

Table 1

Parameters of prepared MWCNT ink

Parameter	**Unit**	**Value**
Viscosity @ $25^\circ\mathrm{C}$	mPa s	5–6
Surface tension	mN/m	30
Density	$\mathrm{g/cm^3}$	~ 1

The inkjet printing was carried out by using Fujifilm Dimatix Materials Printer (DMP-2800) equipped with a 10-pL drop cartridge (DMC-11610). Parameters for printing were tailored by adjusting jetting voltage, frequency, viscosity waveform, drop spacing $(25\,\mu\mathrm{m})$ for a drop size $(35\,\mu\mathrm{m})$. The substrate and the cartridge were used at room temperature. The substrate used for printing is a polycarbonate (PC) sheet (Lexan 8B35E) from Sabic.

2.2. Surface resistance measurement of deposited ink layers

A profile of five CNT-ink-printed layers on a PC sheet was carried out with an interferometer to estimate the thickness of the CNT's film which is less than $50\,\mu\mathrm{m}$. Figure 1a shows a sample of the CNT-ink (1 wt%) printed patches, and Fig. 1b shows scanning electron microscopy (SEM) images of the scratched printed surface, revealing the evenly distributed and entangled carbon nanotube fillers inside the inked layer. A similar SEM image was obtained for ten printed layers, revealing a similar uniform and smooth surface, but it is not shown here for sake of brevity. Inkjet-printed samples were analyzed without further preparation in a FEGSEM Ultra55 instrument (Carl Zeiss). Images were acquired with the SmartSEM software (Carl Zeiss, Germany) at different acceleration voltages ranging between 3 keV and 15 keV, using InLens and SE2 detectors.

Fig. 1

a Five-layer printed pattern of CNT-ink (1 wt%) on polycarbonate sheet, **b** SEM image of scratched printed CNT-ink showing carbon nanotube nanofiller

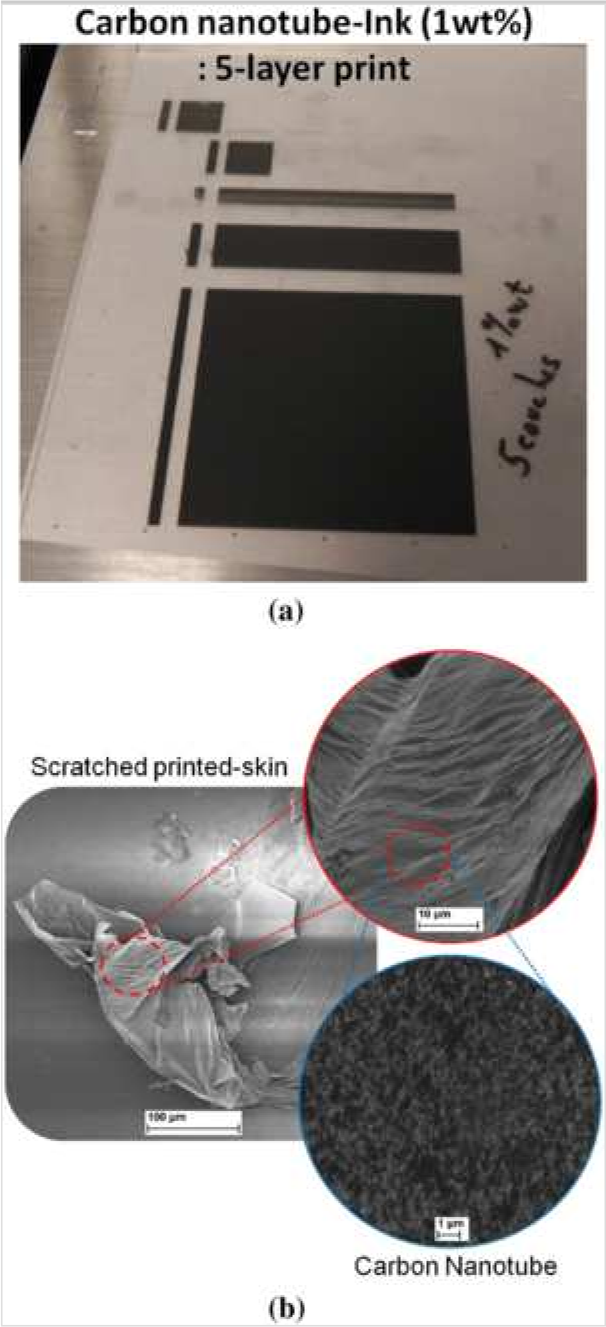

As shown in Fig. 1a, different strip lengths of CNT-ink patterns (1 wt%) were printed on polycarbonate Lexan sheets, having 10, 8, 5, 3, 2 printed layers for the surface resistance measurement. According to [47], each printed layer was annealed in a drying oven at $85\,^{\circ}\mathrm{C}$ for 1 h to achieve a uniform surface resistance. For the measurement, silver paste was applied at the end of each printed patch as probe contact and the measurement was conducted on several samples for averaging the surface resistance $R_{\mathrm{s}}(\Omega/sq.)$, calculated from measured resistance R as :

$$R_s = \frac{R}{w\, l} = \frac{1}{\sigma\, t} \tag{1}$$

where w, l are width and length of the printed patches and σ, t are the conductivity and total thickness of printed CNT film, respectively. Figure 2 shows that despite the reduced number of data points, the measured surface resistance R_s follows well a 1 / n trend, where n is the number of printed layers, in accordance with theoretical equation (1) since the thickness t is proportional to n. As n increases, the number of conductive paths available for electron transport through the thin CNT film increases as well, resulting in improved conductivity and lowered resistivity.

Fig. 2

Measured surface resistance R_s versus number n of printed layers

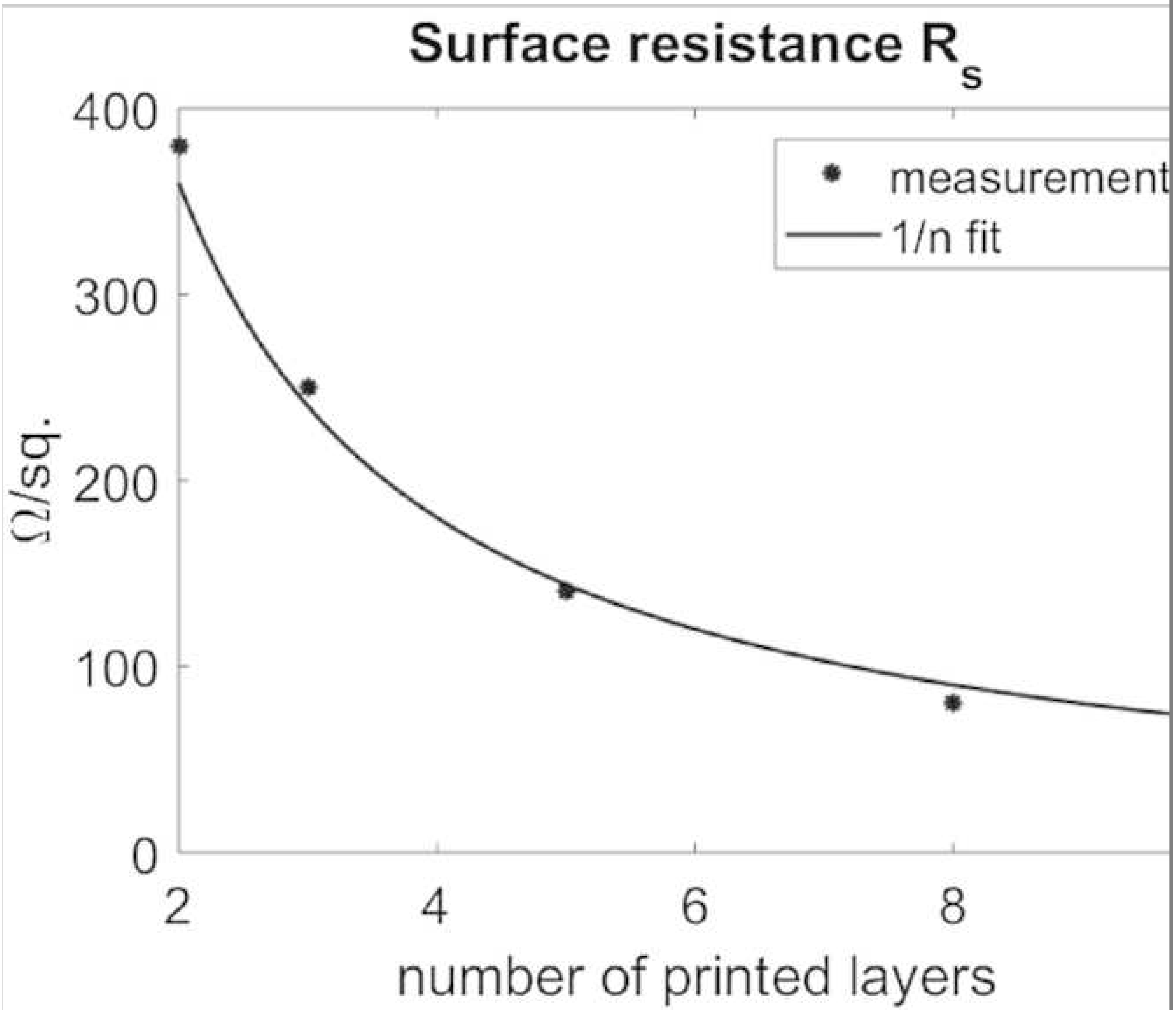

2.3. Microwave characterization

The UWMA was characterized in the 5–50 GHz frequency range using a waveguide method detailed in [48, 49] with an Agilent PNA-X vector network analyzer (VNA). The absorber was sandwiched between waveguide flange ports connected to the VNA via coaxial cables in order to measure the scattering parameters S_{11} and S_{21}, which were used to evaluate the reflectivity and absorption performances of the absorber, respectively. S_{21} represents the transmission of the signal from the input to the output of the structure under scope, while S_{11} corresponds to the reflection of the signal at input of the structure.

3. Results and discussion

3.1. Topology of FSS absorber

Figure 3 presents the schematic structure of the proposed ultra-wideband microwave absorber (UWMA) and its unit cell simulated using CST Microwave Studio software. Resistive FSSs were laminated between two $125\ \mu\mathrm{m}$ thin polycarbonate (PC) films. Then, these two laminates were sandwiched between three low-dielectric substrate spacers (Rogers 5880, $\varepsilon = 2.2$) having thicknesses (d_1, d_2, d_3) and finally backed by a copper ground plane. The top designed FSS, having surface resistance R_{S1}, is a mesh-grid enclosing Jerusalem cross (JC), while the bottom FSS (R_{S2}) consists in a mesh-grid enclosing a square-ring and a cross-dipole. These FSSs were first simulated alone for determining their resonant frequencies responsible for zero reflection. Resulting values selected from Fig. 2 have surface resistance $R_{S1} = 160\ \Omega/sq$ (top) and $R_{S2} = 80\ \Omega/sq$ (bottom). The whole structure was then simulated using the same software to achieve a reflectivity lower than -15 dB in a large frequency range between 5 and 50 GHz.

Fig. 3

a Schematic structure of ultra-wideband microwave absorber (UWMA), **b** resistive FSS for top and bottom CNT-inked layer of unit cell, **c** perspective view of constituent layers in the structure. Dimensions in the structure are: $a_x = a_y = 9.0$, $d_1 = 2.0$, $d_2 = 1.5$, $d_3 = 1.0$, $w_1 = 9$, $w_2 = 6.43$, $w_3 = 2.3$, $l_1 = 9$, $l_2 = 6.93$, $l_3 = 3.0$. Units are in mm. The thickness of the various layers is not shown in scale in scheme **a** to ensure better visibility

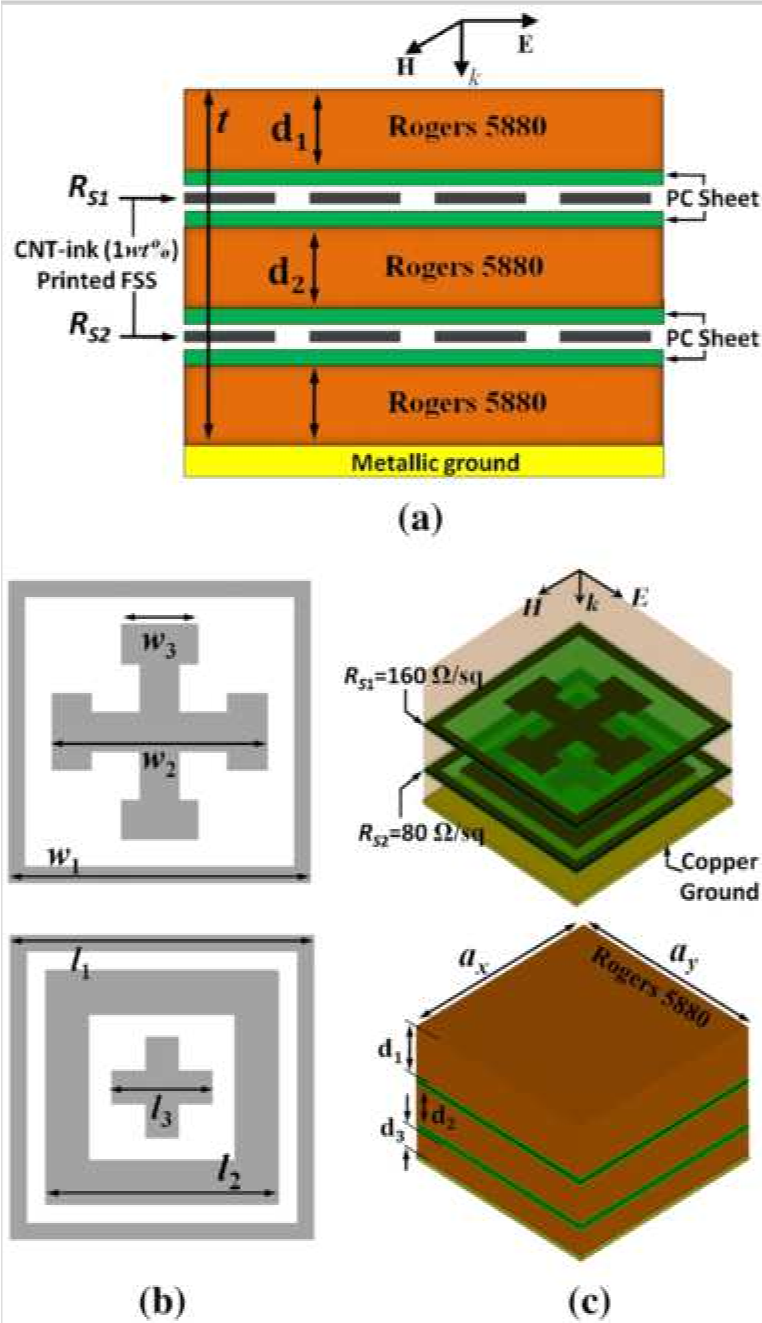

3.2. Equivalent circuit

The equivalent circuit model proposed for the UWMA is shown in Fig. 4. Figure 4b represents the circuital contribution of individual layers to the equivalent circuit diagram of the UWMA as shown in Fig. 4a.

Fig. 4

a Schematic layer representation of UWMA, where yellow represent Rogers spacers and grayscale PC layers. (Thicknesses of layers are not shown in scale for sake of visibility.) **b** Equivalent circuit of FSS1 and FSS2, each sandwiched between two polycarbonate (PC) layers

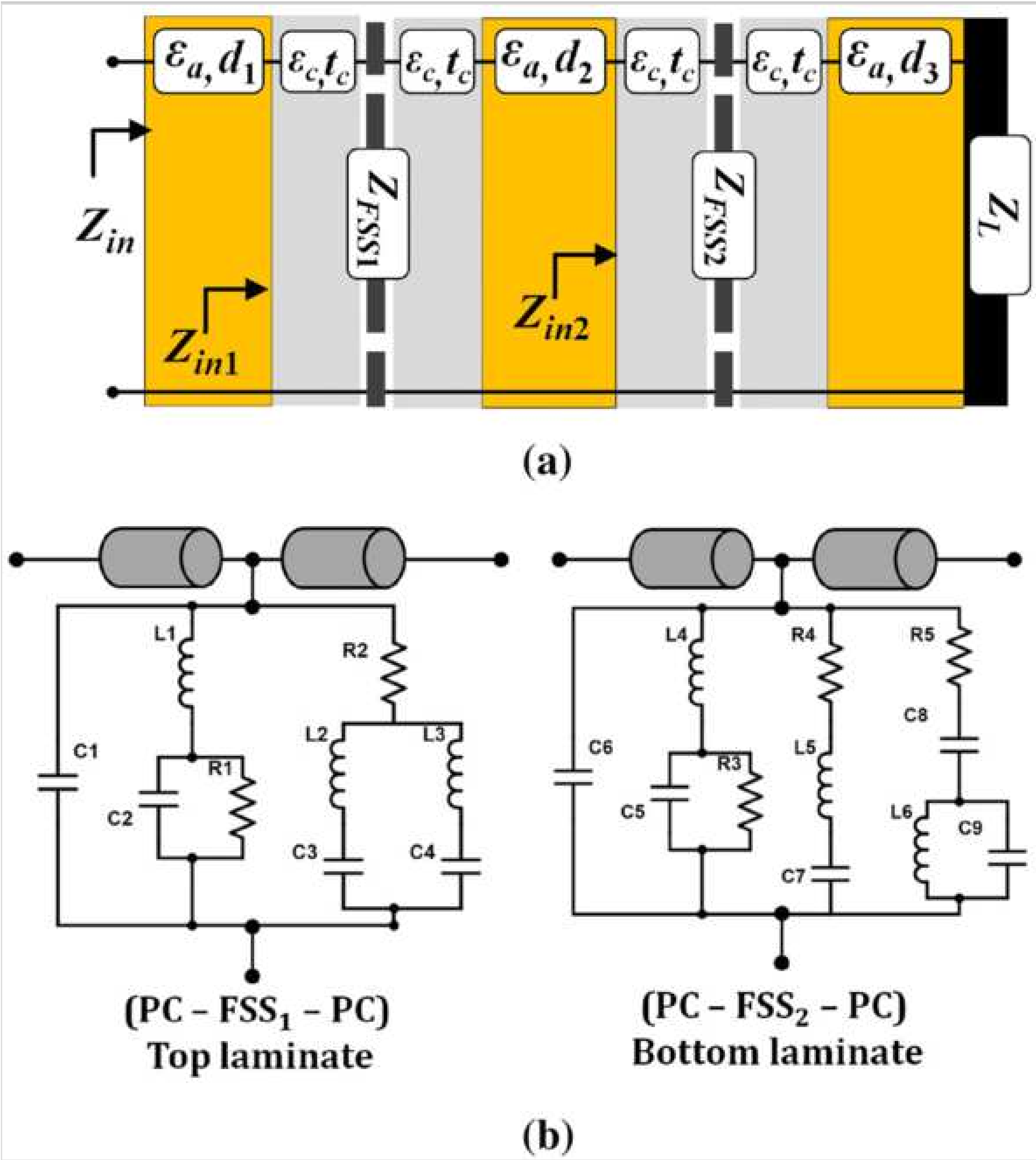

In the equivalent circuit model, the top and bottom FSS are made of series and parallel combination of inductor L, capacitor C and resistor R elements; their values are extracted in MATLAB. Free-space standing FSS is simulated for top (Z_{FSS1}) and bottom (Z_{FSS2}) without polycarbonate film cover; then, its impedance is extracted from simulated S parameters as [26]

$$Z_{\mathrm{FSS}} = \frac{Z_{\mathrm{o}}(1+S_{11})}{2S_{11}} \tag{2}$$

where $\mathrm{Z_o} = 377\ \Omega$ is the free-space impedance. The equivalent circuit model is simulated later in CST (Circuit Design Studio) as well as the reflection coefficient obtained according to the transmission-line approach. It is then compared with the simulated reflectivity in CST Microwave Studio as shown in Figs. 5 and 6. The transfer matrix model approach used for the modeling is as follows [25, 35]. The total transfer matrix of the multilayered structure of Fig. 4a can be expressed as the product matrix of the transfer matrices associated with each layer of the structure:

$$\overline{\overline{T}}_{\mathrm{tot}} = \begin{bmatrix} AB \\ CD \end{bmatrix} = \overline{\overline{T}}_1 \overline{\overline{T}}_{PC} \overline{\overline{T}}_{\mathrm{FSS1}} \overline{\overline{T}}_{PC} \overline{\overline{T}}_2 \overline{\overline{T}}_{PC} \overline{\overline{T}}_{\mathrm{FSS2}} \overline{\overline{T}}_{PC} \overline{\overline{T}}_3 \tag{3}$$

The chain matrix $\overline{\overline{T}}_i$ of layer i expresses as, for Rogers layers 1, 2, 3, and for PC layers

$$T_i = \begin{bmatrix} \cosh(\gamma_i d_i) & Z_{ci}\sinh(\gamma_i d_i) \\ 1/Z_{ci}\sinh(\gamma_i d_i) & \cosh(\gamma_i d_i) \end{bmatrix} \tag{4}$$

with $\gamma_i = \jmath\, 2\pi f \sqrt{\varepsilon_{ei}}\ /c_{\mathrm{o}}$ the propagation constant in layer i, $Z_{ci} = 377\Omega/\sqrt{\varepsilon_{ei}}$ its characteristic impedance associated with propagation, where ε_{ei} is the permittivity of layer i and d_i its thickness according to Table 2.

Table 2

Nomenclature, composition and electromagnetic parameters of the five layers forming the UWMA

Layer	Composition	ε	Thickness (mm)
1	Rogers 5880	2.2	0.25
2	Lexan 8B35E (PC)	2.9	2×0.125
3	Rogers 5880	2.2	1.5
4	Lexan 8B35E (PC)	2.9	2×0.125
5	Rogers 5880	2.2	1.0

The transfer matrix of the two FSSs has the expression:

$$\overline{\overline{T}}_{\mathrm{FSSi}} = \begin{bmatrix} 1 & 0 \\ 1/Z_{\mathrm{FSSi}} & 1 \end{bmatrix} \quad (5)$$

where Z_{FSSi} is the impedance for the top (FSS1) and bottom (FSS2) sheets given by (2) which expresses as:

– for top FSS1

$$Z_{\mathrm{FSS1}} = T_1 + T_2 + T_3 \quad \text{6a}$$

$$T_1 = 1/\jmath\omega C_1 \quad \text{6b}$$

$$T_2 = \jmath\omega L_1 + \frac{1}{1/R_1 + \jmath\omega C_2} \quad \text{6c}$$

$$T_3 = R_2 + \frac{1}{1/(\jmath\omega L_2 + 1/(\jmath\omega C_3)) + 1/(\jmath\omega L_3 + 1/(\jmath\omega C_4))} \quad \text{6d}$$

– for bottom FSS2

$$\begin{aligned} Z_{\mathrm{FSS2}} &= B_1 + B_2 + B_3 + B_4 \\ B_1 &= 1/\jmath\omega C_6 \end{aligned} \quad \text{7a}$$

$$B_2 = \jmath\omega L_4 + \frac{1}{1/R_3 + \jmath\omega C_5} \quad \text{7b}$$

$$B_3 = R_4 + \jmath\omega L_5 + 1/(\jmath\omega C_7) \quad \text{7c}$$

$$B_4 = R_5 + 1/(\jmath\omega C_8) + \frac{1}{1/(\jmath\omega L_6) + \jmath\omega C_9} \quad \text{7d}$$

Table 3

Values for the elements of the equivalent circuit in Fig. 4b

Z_{FSS1}	Z_{FSS2}
$L_1 = 30.177\,\mathrm{nH}$	$L_4 = 2.492\,\mathrm{nH}$
$L_2 = 5.2361\,\mathrm{nH}$	$L_5 = 22.8267\,\mathrm{nH}$
$L_3 = 2.5886\,\mathrm{nH}$	$L_6 = 1.272\,\mathrm{nH}$
$C_1 = 2.3972\,\mathrm{fF}$	$C_5 = 20.8611\,\mathrm{fF}$
$C_2 = 2.6108\,\mathrm{fF}$	$C_6 = 21.9840\,\mathrm{fF}$
$C_3 = 1.5562\,\mathrm{fF}$	$C_7 = 0.7225\,\mathrm{fF}$
$C_4 = 14.8281\,\mathrm{fF}$	$C_8 = 1.2023\,\mathrm{fF}$
	$C_9 = 10.3632\,\mathrm{pFR}$
$R_1 = 5600\Omega$	$R_3 = 680\,\Omega$
$R_2 = 360\Omega$	$R_4 = 280\,\Omega$
	$R_5 = 130\Omega$

Lumped element data provided in Table 3 for FSS1 and FSS2 are determined from the MATLAB fitting algorithm. It fits the impedance of the sandwich PC/FSSi/PC structure obtained from the simulation of their S parameters using (2) with the impedance of the equivalent circuit of Fig. 4.

3.3. Design constraints

We consider the design constraints as follows:

1. The impedance of the FSS can be represented as the combination of an LC circuit and resistors as given by (4) and (5). The surface current generated due to incident EM wave flows through the resistive imperfect conductor formed by the ink-printed FSS, minimizes the scattered energy and contributes to total losses in the composite. Hence, the wideband absorber can be realized through a proper choice of the surface resistance and FSS shapes geometry [27]. The surface resistance (R_s) can be tuned to obtain narrowband to wideband absorption;

2. A low permittivity value for Rogers spacers and PC Lexan films is preferred since a higher permittivity reflects the incident EM wave, preventing absorption [24];

3. Minimal reflection must be < -15 dB, or absorption is $> \ 90\%$ in the whole frequency range;

4. Minimal number of layers in the multilayer absorber in order to minimize thickness and ensure compactness;

5. The magnitude of reflection coefficient $(\mathit{\Gamma})$ can be expressed as [34, 35]:

$$|\mathit{\Gamma}| = \left|\frac{Z_{\text{in}} - Z_{\text{o}}}{Z_{\text{in}} + Z_{\text{o}}}\right| \tag{8}$$

where $\mathrm{Z_{in}}$ is the input impedance as shown in Fig. 4a. The absorption from a metal-backed absorber can be estimated as

$$A = 1 - |\mathit{\Gamma}|^2 \tag{9}$$

To achieve an excellent absorption level, it is important that the imaginary part of input impedance $\mathrm{Z_{in}}$ goes to zero and its real part should matched the free-space impedance, i.e., $\Re(\mathrm{Z_{in}}) = \mathrm{Z_o}$ and $\Im(\mathrm{Z_{in}}) \approx 0$

The input impedance can be easily related to the elements of the global transfer matrix $\overline{\overline{T}}_{\text{tot}}$ [50] :

$$Z_{\text{in}} = \frac{AZ_{\text{o}} + B - CZ_{\text{o}}^2 - DZ_{\text{o}}^2}{AZ_{\text{o}} + B + CZ_{\text{o}}^2 + DZ_{\text{o}}^2} \tag{10}$$

3.4. Simulations

The equivalent circuit model (3–10) is simulated according to the transmission-line approach, and the resulting reflectivity (8) is then compared with the simulated reflectivity in CST Microwave Studio as shown in Fig. 5. An excellent agreement is observed which validates the equivalent circuit model. The obtained reflectivity is below - 15 dB over most part of the frequency range, in accordance with the design constraint n°3. Therefore, the equivalent circuit can be used to predict the absorption using (8) and (9), as shown in Fig. 6a.

Fig. 5

Reflectivity Γ of the UWMA calculated using CST Microwave Studio and transfer matrix multiplication model(3)

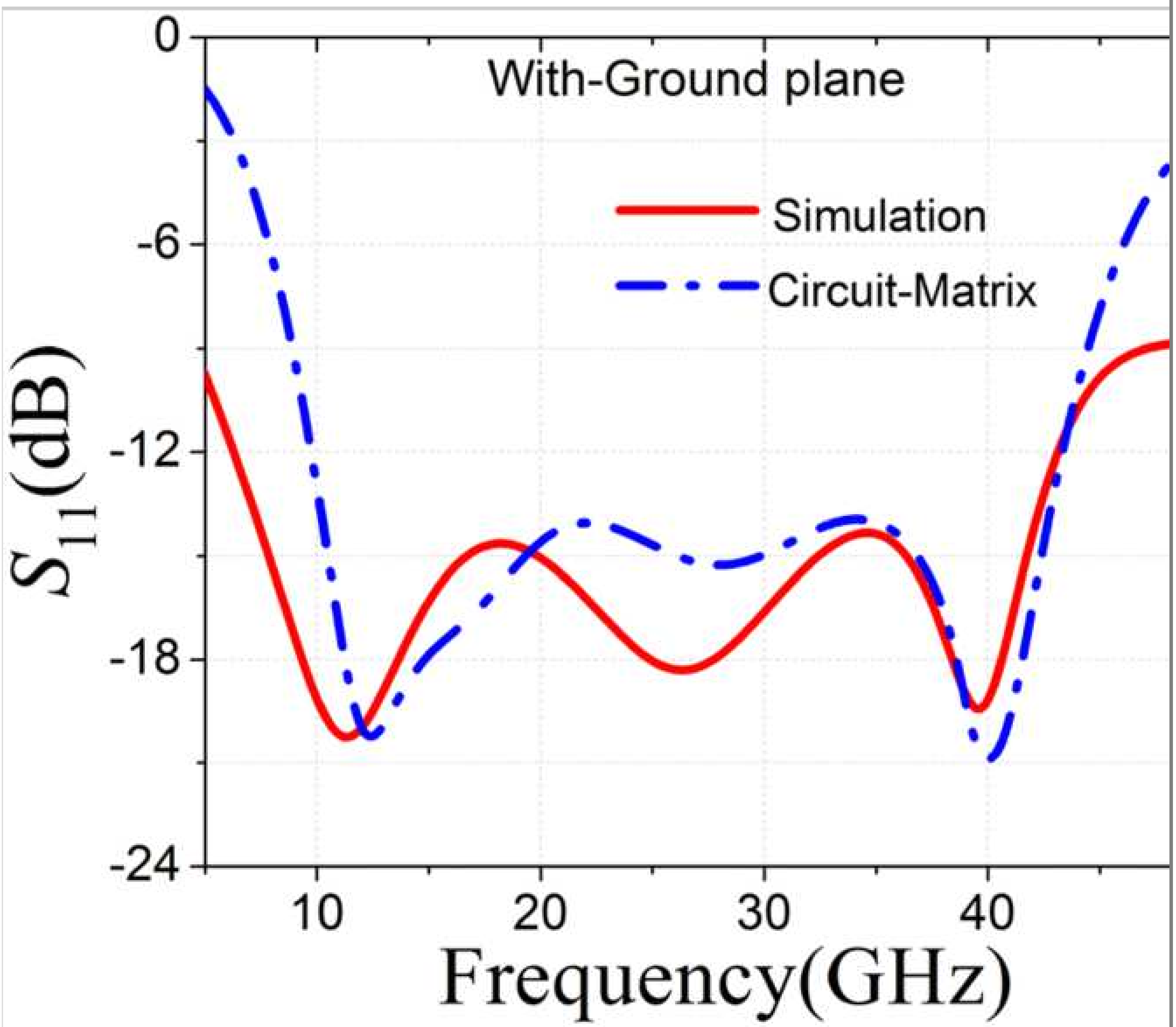

Fig. 6

a Absorption and reflection performance **b** Definition of layers and interfaces for the analysis of resonances in the multilayer

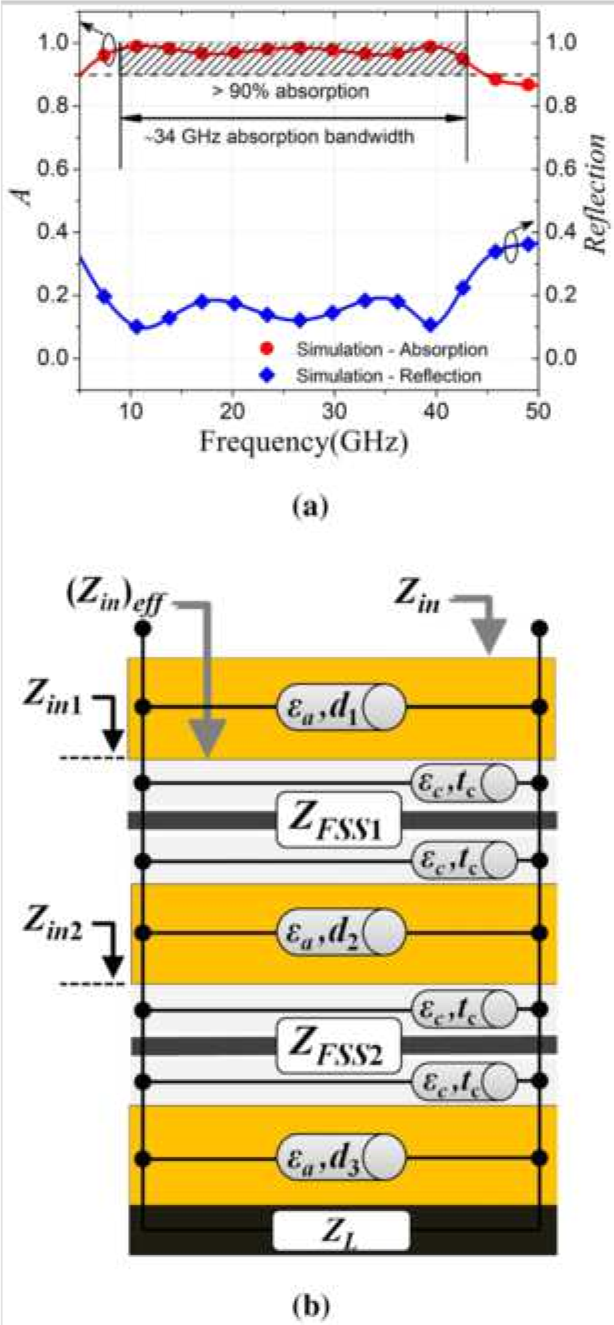

As next step, Fig. 7a shows that three reflection resonances f_1, f_2, f_3 occur in the frequency band 5–50 GHz range and calculated absorption is around 90% between 7.30 and 41.95 GHz corresponding to an absorption bandwidth of $\approx$ 34 GHz and a fractional bandwidth of $\approx$ 137% as shown in Fig. 6a. To understand the origin of the three resonances at f_1, f_2, f_3, we examined the input impedances at interfaces Z_{in1} and Z_{in2} as shown in Fig. 6b.

Fig. 7

Input impedances defined at Fig. 6a real parts **b** imaginary parts

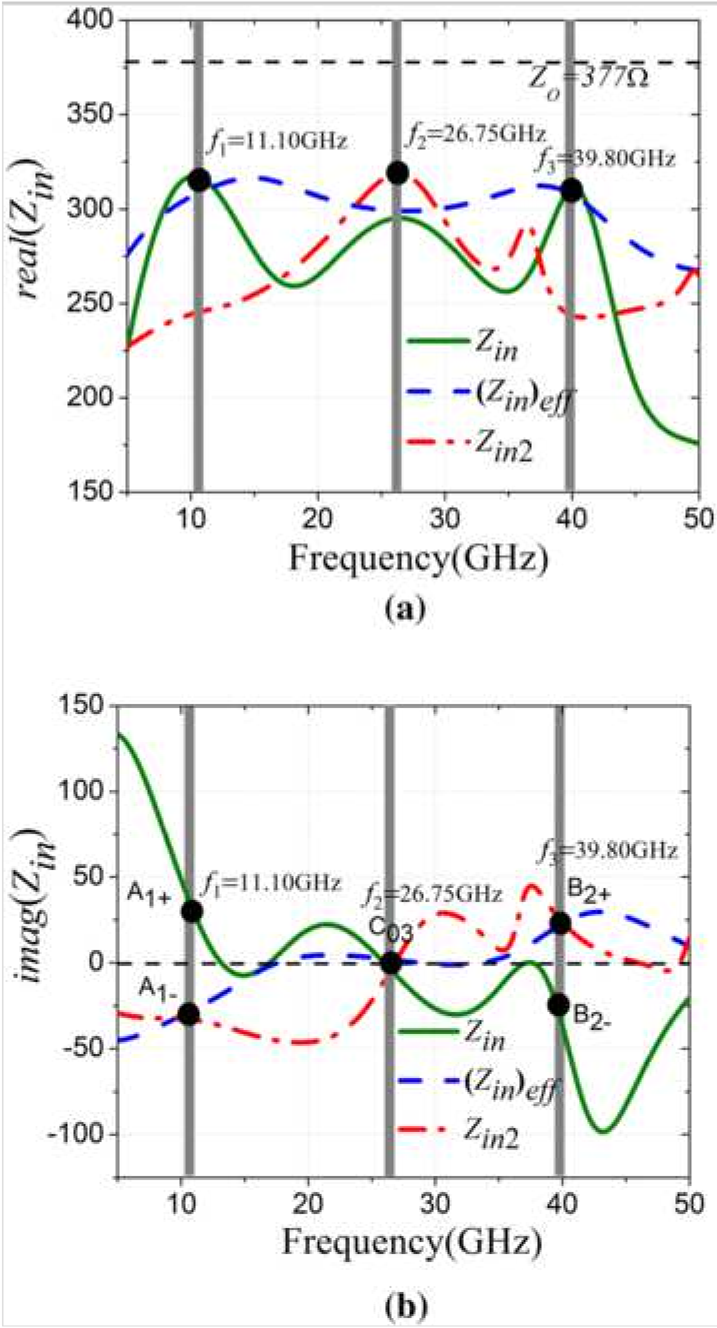

AQ2

In a classical Salisbury screen, the resonance occurs when the inductive impedance of the grounded dielectric substrate and the capacitive impedance of the resistive screen have same magnitude and opposite sign. The imaginary part of the input impedances cancels each other or goes to zero, and real part contributes to the losses. Since both reactances vary with the frequency, the compensation happens at only one resonant frequency at which the value of both reactances is equal and opposite. Applying this concept to the multiresonant structures, we can write the resonance condition for the peaks in the proposed UWMA as the fact that three resonances occur when the imaginary part of the input impedances $\Im(Z_{\text{in}})$ or the reactance of the input impedances exactly cancels each other [51], i.e.,

$$\Im(Z_{\text{in}}) + \Im(Z_{\text{in eff}}) = 0 \tag{11}$$

where Z_{in} represents the input impedance at air–absorber interface, while $Z_{\text{in eff}}$ shows the effective input impedance at the top FSS and can be seen intuitively as $Z_{\text{in eff}} = Z_{\text{in1}} + Z_{\text{in2}}$ which represents the total input impedance (Fig. 6b). The resonance frequencies are shown related to these impedances in Fig. 7a, b. Hence, from the above equation, two conditions which lead to the three resonance peaks can be written as:

$$(1) \quad \Im(Z_{\text{in}}) \approx -\Im(Z_{\text{in eff}}) \neq 0 \tag{12a}$$

$$(2) \quad \Im(Z_{\text{in}}) \approx 0 \quad \Im(Z_{\text{in eff}}) \approx 0 \tag{12b}$$

Condition (1) shows that the reactance parts of the input impedance, which may be either inductive or capacitive, cancel each other since they have same magnitude with opposite sign.

Condition (2) shows that the value of imaginary part of the input impedances approaches to zero [51].

In Fig. 7a, b, it can be observed that the input impedances satisfy well the two conditions at three resonance peaks f_1, f_2, f_3 and high resistance real part contributes to suppression of EM wave. From Fig. 7, following observations are in line with the two conditions (12) for resonances:

1) At first resonance f_1: points A_{1+} and A_{1-} represent the reactance part of input impedances Z_{in} and $Z_{\text{in eff}}$ which can be either inductive or capacitive, having the magnitudes $A_{1+} = 26.15\ \Omega$ and $A_{1-} = -26.80\ \Omega$ respectively, which satisfies the condition (12a) as A_{1+} and A_{1-} cancel

each other resulting in a reflection deep at f_1 as shown in Fig. 7b.

2) At second resonance f_2: point C_{03}, the condition (12b) applies well where the reactance of input impedances approaches to zero, i.e., $\Im(Z_{\mathrm{in}}) \approx 0.5\ \Omega$ and $\Im(Z_{\mathrm{in\ eff}}) \approx 0.1\ \Omega$ resulting in reflection deep at f_2 = 26.75 GHz.

3) At third resonance f_3: points B_{2+} and B_{2-} satisfy the condition (12a), where the magnitude of the reactances is $B_{2+} = 21.22\ \Omega$ and $B_{2-} = -21.60\ \Omega$, and hence cancel each other as $B_{2+} \approx -B_{2-}$, and as a result the reflection deep appears at f_2 26.75 GHz.

From Fig. 7a, it is pointed out that at every frequency point, only the significant magnitude of the real part of the impedances contributes to the absorption losses when the resonance condition is satisfied and this multiresonant nature allows to achieve the ultra-wideband absorption performance.

Since these three frequency peaks represent the multiresonant nature of the absorbing structure and contribute to improving the absorption bandwidth, cascading more resonant FSS structures may increase further the performance of the structure [25, 35]. Indeed, FFSs can be added in the equivalent circuit, having parameters extracted from their CST-simulated S parameters, in order to tailor the number and positions of the resonant frequencies and finally adjust the bandwidth.

3.5. Experimental validation

A sheet of $100 \times 100\mathrm{mm}^2$ was printed on PC films (Fig. 8a, b) using the method described in Sect. 2.1 and was then sandwiched between the Rogers 5880 dielectric spacers to fabricate the absorber (Fig. 3). The scattering parameters S_{11} and S_{21} of the UWMA were measured as illustrated in Fig. 9d using the waveguide method described in Sect. 2.3, with and without ground plane.

Fig. 8

Photograph of carbon nanotube ink (1 wt%)-printed FSS on polycarbonate film for left: top FSS and right: bottom FSS (inset: enlargement of unit cell portion)

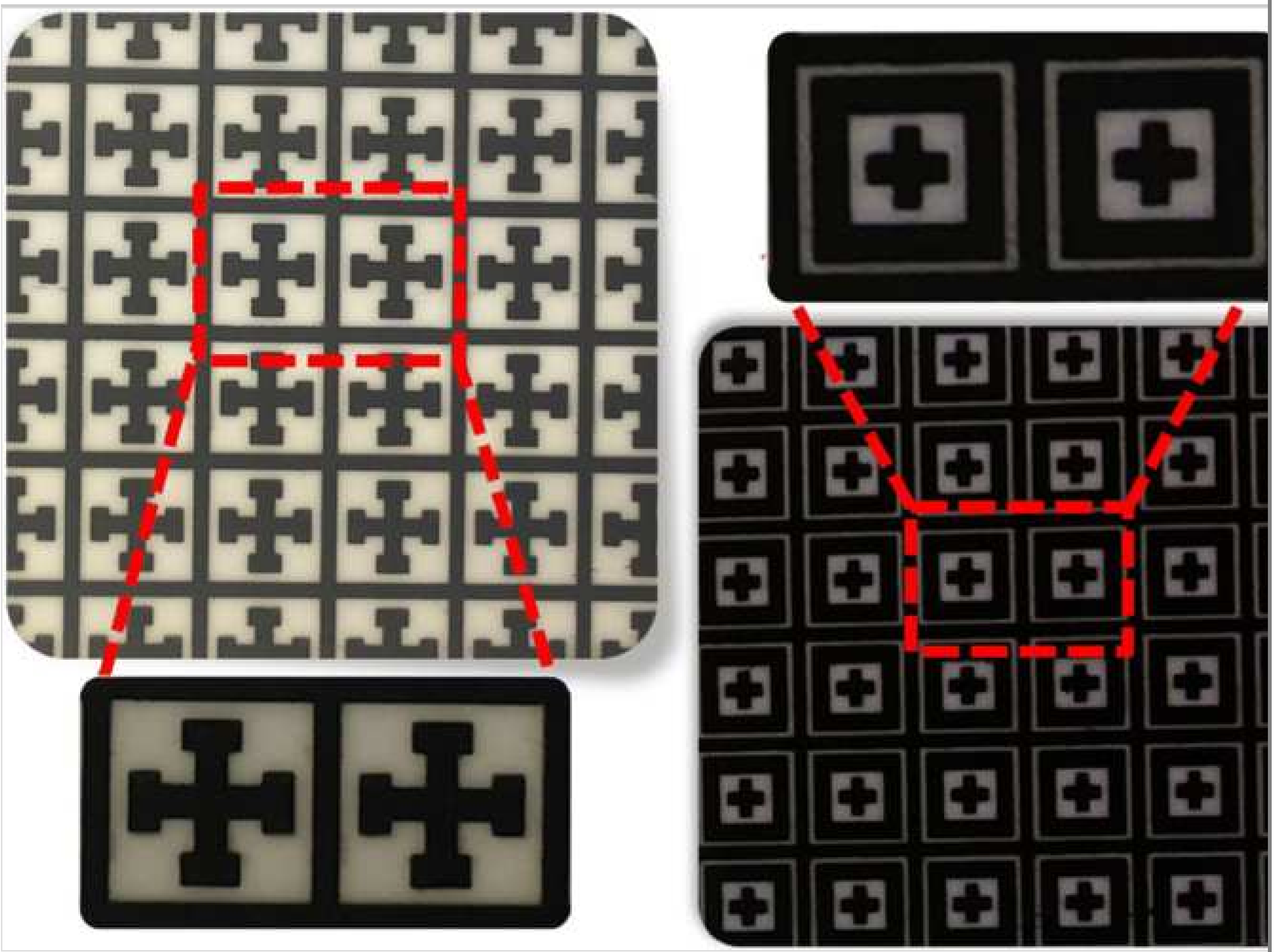

Figure 9a shows measured and simulated reflection coefficient S_{11} for UWMA absorber with ground plane (8), Fig. 9b, c shows reflection S_{11} and transmission S_{21} for UWMA composite without ground plane [configuration shown in inset of (c)], while Fig. 9d is a representative illustration of the waveguide measurement setup. An excellent agreement is observed between measured and simulation results. It is observed in Fig. 9a that measured and simulated reflectivity S_{11} is about -15 dB between 7.85 and 41.85 GHz, corresponding to ultra-wide band absorption. In addition, Fig. 9c shows the measured transmission coefficient S_{21} of UWMA composite without ground plane. Again a good agreement is found with simulation results, which confirms the validity of our approach.

Fig. 9

Comparison between simulation and measurement of UWMA based on CNT-resistive ink **a** reflection coefficient S_{11} with ground plane, **b** S_{11} without ground plane, **c** transmission coefficient S_{21} without ground plane (see configuration in inset), **d** representative illustration of waveguide measurement setup

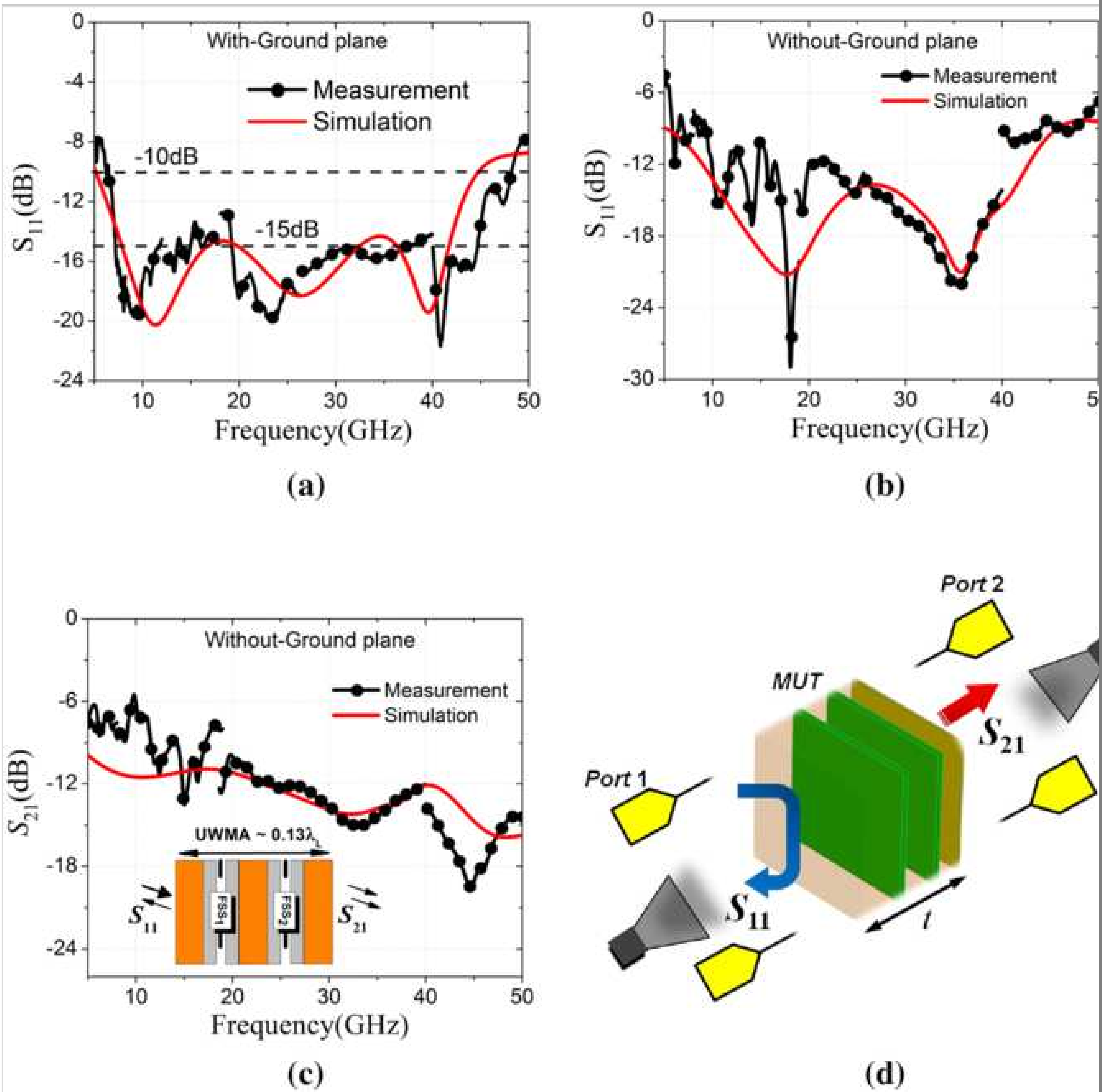

The discrepancies in measured data as compared to simulation can be attributed to instrumental mismatch, handling and other experimental factors accounting for standard operating procedures. In particular, the discontinuities between curves observed at 18, 26 and 40 GHz correspond to changing the waveguide size from one frequency band to the other in order to perform the broadband characterization [48].

Figure 10 shows that the absorption magnitude obtained from (9) is above 90% over a 34 GHz bandwidth, i.e., from 7.3 to 41.95 GHz, for an absorber thickness equal to 5.1 mm, which is about 0.13 λ_{L}. (λ_{L} is the wavelength at lower frequency of the considered band.) Also, the corresponding fractional bandwidth calculated as FB = $(f_{\mathrm{H}} - f_{\mathrm{L}})/(f_{\mathrm{H}} + f_{\mathrm{L}})$, where f_{L} and f_{H} are the lower and higher frequencies of the considered band respectively, is about 137%. Again, a good agreement is found with simulation results, which validates our approach further.

Fig. 10

Absorption performance of the CNT-ink absorber

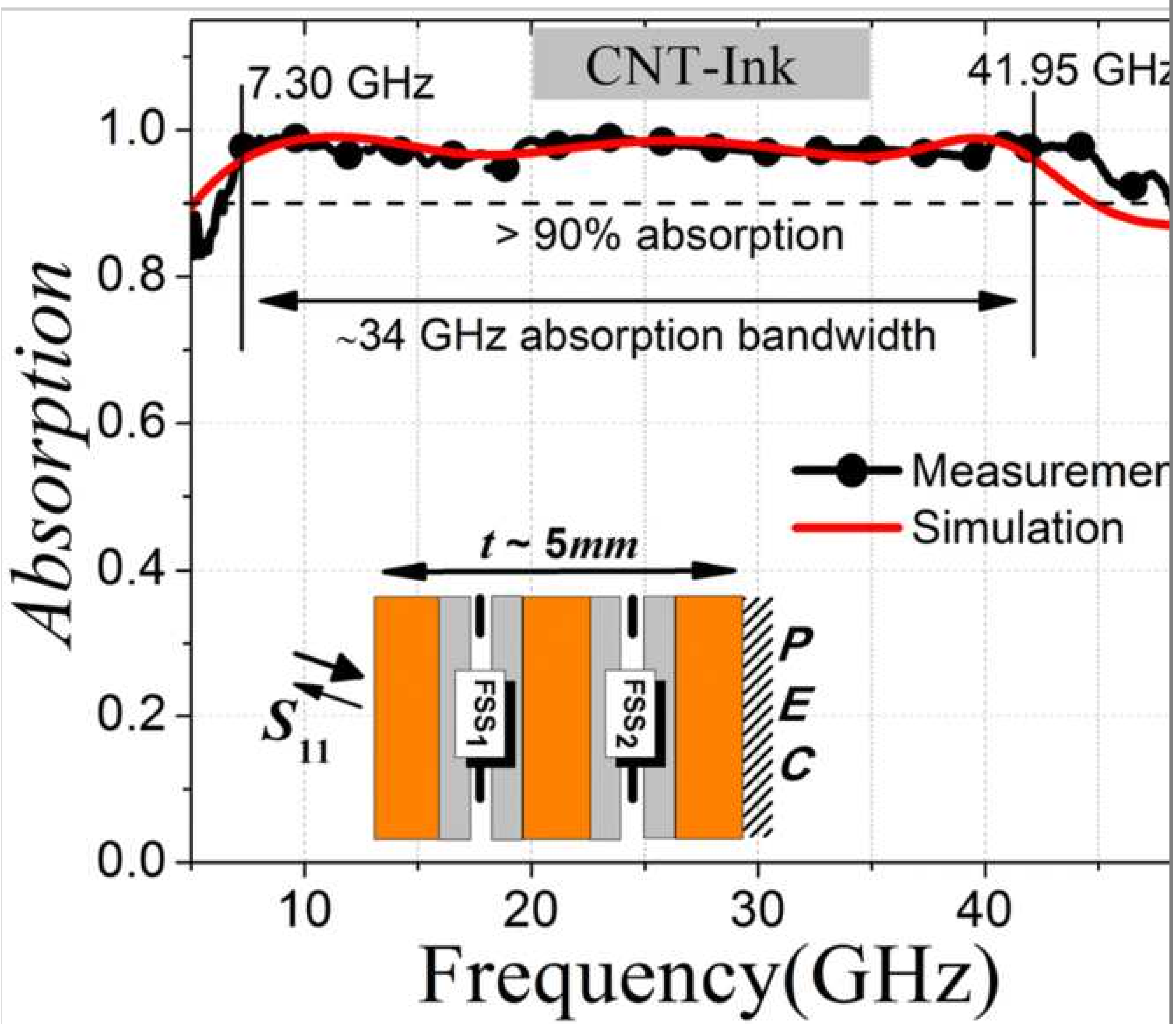

Figure 11 shows the simulated E_y electric field component propagating through the structure at 9 GHz where almost all the incident EM wave enters the structure due to impedance matching and dissipates inside the medium due to resistive FSSs. A similar behavior is also observed at 40 GHz, but is not shown here for sake of brevity.

Fig. 11

Electric field (E_y) computed through unit cell structure at 9 GHz at normal incidence

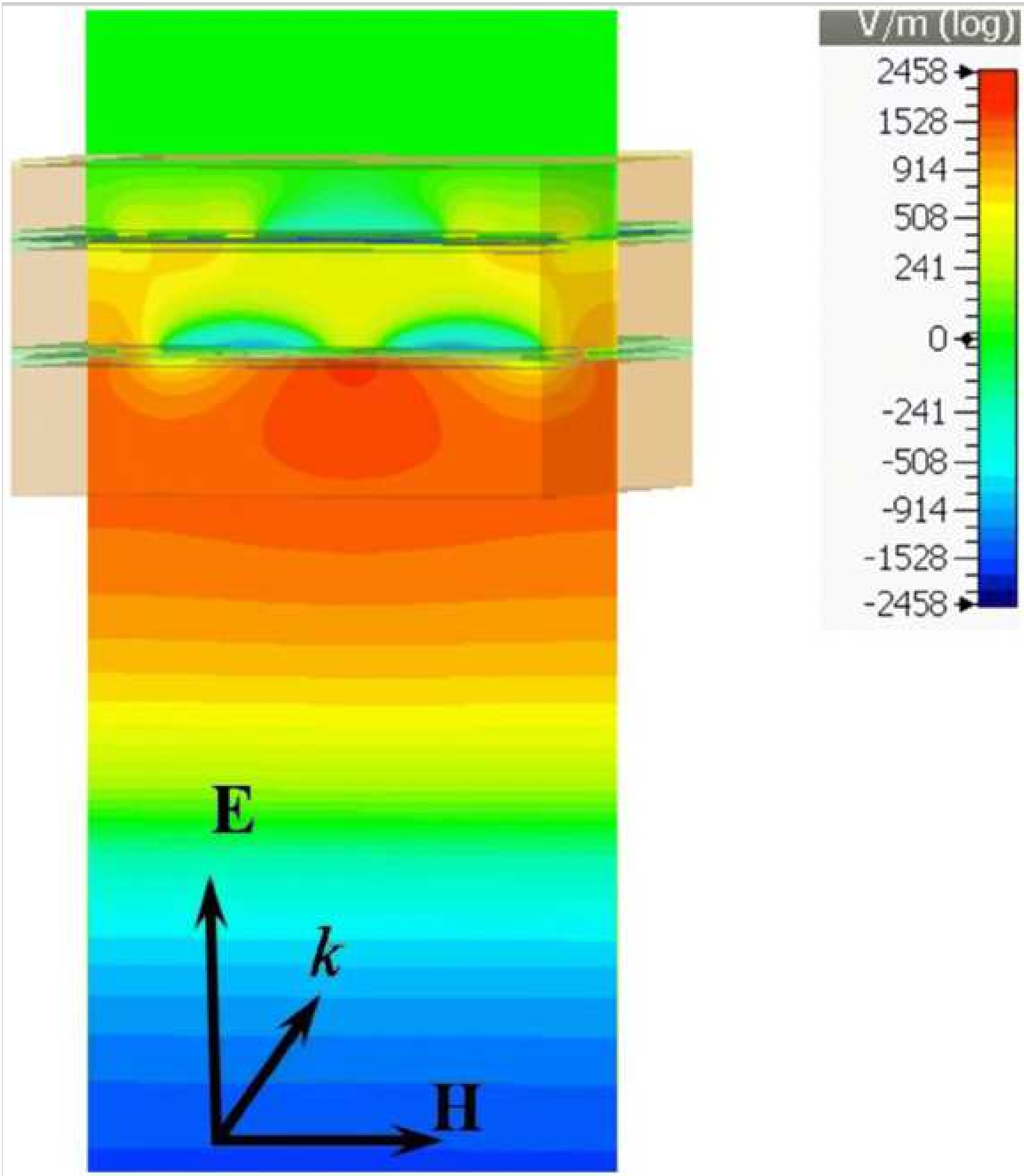

3.6. Angular stability

Furthermore, it is important to study the angular stability of the reflectivity of the UWMA absorber under oblique incidence. Owing to the excellent agreement observed at Figs. 9 and 10 between measurements and CST simulations, the software is used to simulate the reflectivity of the absorber for both transverse magnetic (TM) and transverse electric (TE) polarization and under various incidences of electromagnetic (EM) wave, as shown in Fig. 12. It is observed that the reflectivity performance is better under TM than under TE polarization, which may be related to the different ways of wave dissipation, impedance mismatch, etc. Overall, the reflectivity has acceptable performance of about -14 to -15 dB up to $\theta = 40°$ incident angle for both polarizations in a large frequency band.

Fig. 12

Simulated reflectivity at different incident angles of EM wave **a** TE polarization, **b** TM polarization

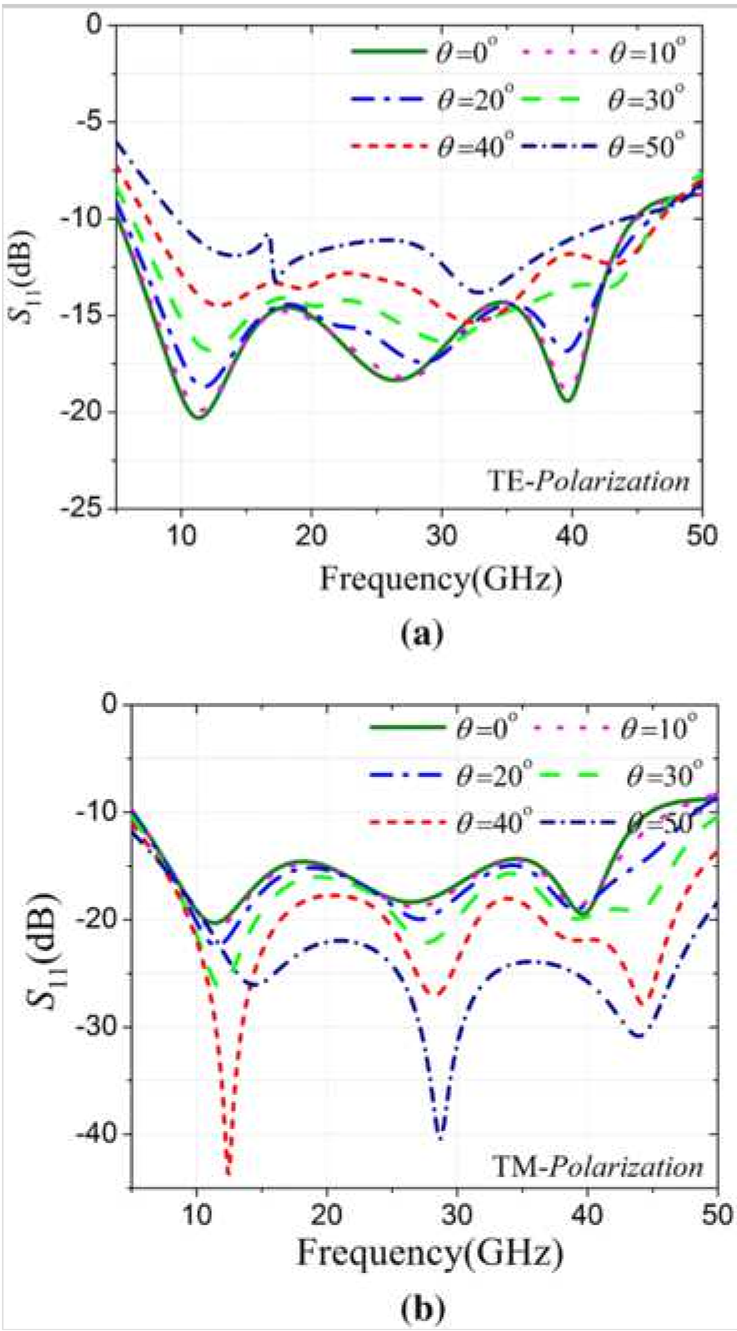

3.7. Assessment of performances

Table 4 shows the comparison in terms of bandwidth and thickness with other state-of-the-art broadband absorbers. It is evident that the proposed UWMA stands out in terms of absorption bandwidth and compacity since its calculated figure of merit FOM = FB/ (thickness expressed as fraction of λ_L) shows better performance.

Maximizing the absorption bandwidth usually increases the corresponding absorber thickness so it is not trivial to design a thin- and wideband absorber. However, there exists a physically realizable minimum theoretical thickness (d_m), expressed as a function of reflectivity, that allows to achieve a given required absorption performance [28]:

Table 4

Comparison with state of the art

References	**Absorption bandwidth (GHz)**	**Fractional bandwidth FB (%)**	**FOM**	**Absorber thickness in mm (in λ_L)**	**Unit cell type**
[52]	7.66	69	460	6.0 (0.15 λ_L)	Single layer resistive FSS
[26]	9.3	62	861	2.0 (0.072 λ_L)	Single layer resistive FSS
[53]	10	77	785	3.5 (0.093 λ_L)	2 Layer resistive square patch
[36]	7.5	129	1466	13.2 (0.088 λ_L)	2 Loops with resistors
[54]	30.4	137	1522	3.8 (0.09 λ_L)	3 Layer resistive square patch
[22]	31.39	165	1031	14.5 (0.16 λ_L)	Multiresistive square patch
This work	33.9	137	1053	5.1 (0.13 λ_L)	Double layer resistive FSS

$$\left|\int_0^{\infty} R(\lambda) d\lambda \leq 2\pi^2 \mu_s d_m\right| \tag{13}$$

where μ_s, d_m and R(λ) are the static permeability, minimum thickness and reflectivity over operational wavelength. Thickness d_m can also be written for minimum thickness in the wavelength limit(λ_{max},λ_{min}) for non-magnetic absorber under normal wave incident as:

$$d_m = \frac{\left|\int_{\lambda_{min}}^{\lambda_{max}} ln(R(\lambda) d\lambda\right|}{2\pi^2} \tag{14}$$

where λ_{max}, λ_{min} are maximum and minimum of the wavelength range of operation. The minimum theoretical thickness estimated from the Rozanov's equation is $d_m = 4.7\,\mathrm{mm}$, and the practically realized absorber is here 5.1 mm thick which is close to the theoretical thickness limit satisfying the Rozanov's condition. Rozanov's limit is a landmark for absorber performance, and its applicability has been explored for a variety of systems.

4. Conclusions

We can state that our CNT-ink-based UWMA combines compacity and wideband absorption through an adequate selection of the number of printed layers, controlling the resistivities of the FSS. The absorber has a fractional bandwidth of 137% and a FOM = 1053, for a thicknesses of only 5.1 mm. An equivalent circuit is derived to explain the resonant origin of the ultra-wideband absorption. The performances are successfully compared to the state-of-the art and the Rozanov limit.

The huge fractional bandwidth obtained confirms that the new UWMA is a highly efficient EMI shielding alternative since absorption constitutes the main shielding mechanism and is obtained at very reduced thickness. Furthermore, its lightweight and ease of fabrication offer promising perspectives for space and aeronautics applications as well as in mobile wireless communications, where compactness is a key issue [55].

Publisher's Note

Springer Nature remains neutral with regard to jurisdictional claims in published maps and institutional affiliations.

Acknowledgements

The authors are grateful to the National Fund for Scientific Research (F.R.S.-FNRS, Belgium) for supporting this research. This work is also supported by the Walloon region, and by the "Communauté Française de Belgique," through the project "Nano4waves" funded by its research program "Actions de Recherche Concertées." Special thanks are also due to Profs. C. Bailly and A. Delcorte for fruitful discussions.

Compliance with ethical standards

Conflict of interest The authors declare that they have no conflict of interest.

References

1. A. Khoshroo et al., J Electroanal. Chem. **823**, 61–66 (2018)
2. J. Amania et al., Anal. Biochem. **548**, 53–59 (2018)
3. H.R. Naderi et al., Appl. Surf. Sci. **423**, 1025–1034 (2017)
4. I.V. Zaporotskova et al., Mod. Electron. Mater. **2**, 95–105 (2016)
5. V.D.N. Bezzon et al., Adv. Mater. Sci. Eng. 21 p (2019)

AQ3

6. S. Revathia et al., Int. J. Electron. Electr. Comput. Syst. **7** (2018)

AQ4

7. J. Pena-Bahamonde et al., J Nanobiotechnol. **16** (2018)
8. G. Zhou et al., Resistive switching memory integrated with amorphous carbon-based nanogenerators for self-powered device. Nano Energy **63**, 103793 (2019)
9. G. Ijeomah et al., Int. J. Nano Biomater. **6** (2016)

10. L. Fekri Aval et al., Heliyon. **4** (2018)

11. A. Bakandritsos et al., FlatChem **13**, 25–33 (2019)

12. X. He et al., Reinforced carbon fiber laminates with oriented carbon nanotube epoxy nanocomposites: magnetic field assisted alignment and cryogenic temperature mechanical properties. J. Colloid Interface Sci. **517**, 40–51 (2018)

13. C. Caloz, T. Itoh, *Electromagnetic Metamaterials: Transmission Line Theory and Microwave Applications: The Engineering Approach* (Wiley, Hoboken, 2016)

14. R. Marques et al., *Metamaterials with Negative Parameters: Theory, Design, and Microwave Applications* (Wiley, Hoboken, 2008)

15. C. Watts et al., Metamaterial electromagnetic wave absorbers. Adv. Mat. **24**, 98–120 (2012)

16. P. Yu et al., Broadband metamaterial absorbers. Adv. Opt. Mater. 1800995 (2018)

17. B. Chambers, Optimum design of a Salisbury Screen radar absorber. IEE Electron. Lett. **30**(16), 1353–1354 (1994)

18. F.Che Seman et al., Design of a salisbury screen absorber using frequency selective surfaces to improve bandwidth and angular stability performance. IET Microw. Antennas Propag. **5**(2), 149–156 (2011)

19. B. Chambers et al., Design of wideband Jaumann radar absorbers with optimum oblique incidence performance. IEE Electron. Lett. **30**(18), 1530–1532 (1994)

20. B.A. Munk et al., On designing Jaumann and circuit analog absorbers (CA absorbers) for oblique angle of incidence. IEEE Trans. Antennas Propag. **55**(1), 186–193 (2007)

21. A. Kazemzadeh, A. Karlsson, Multilayered wideband absorbers for

oblique angle of incidence. IEEE Trans. Antennas Propag. **58**(11), 36370–3646 (2010)

22. A. Kazemzadeh, Nonmagnetic ultrawideband absorber with optimal thickness. IEEE Trans. Antennas Propag. **59**(1), 135–140 (2011)

23. Ye Han et al., A fast and efficient method for design of circuit analog absorbers consisting of resistive square loop arrays. IEEE Trans. Electromagn. Compat. **58**(3), 35–37 (2016)

24. P. Munaga et al., A fractal-based compact broadband polarization insensitive metamaterial absorber using lumped resistors. Microw. Opt. Technol. Lett. **58**(2), 343–347 (2016)

25. E. Yildimy, O. Aydin Civi, Design of a Wideband Radar Absorbing Structure, in Proceedings of 5th European Conference on Antennas and Propagation (EUCAP) (2011)

26. M. Olszewska-Placha et al., A Broadband absorber with a resistive pattern made of ink with graphene nano-platelets. IEEE Trans. Antennas Propag. **63**(2), 565–572 (2015)

27. F. Costa et al., Analysis and design of ultra-thin electromagnetic absorbers comprising resistively loaded high impedance surfaces. IEEE Trans. Antennas Propag. **58**(5), 1551–1558 (2010)

28. K.N. Rozanov, Ultimate thickness to bandwidth ratio of radar absorbers. IEEE Trans. Antennas Propag. **48**(8), 1230–1234 (2000)

29. Z. Jia et al., Laminated microwave absorbers of A-site cation deficiency perovskite La0.8FeO3 doped at hybrid RGO carbon. Compos. Part B **176**, 107246 (2019)

30. G. Wu et al., Interlayer controllable of hierarchical MWCNTs@C@FexOy cross-linked composite with wideband electromagnetic absorption performance. Compos. Part A **128**, 105687 (2020)

31. X. Zhou et al., Synthesis of Fe3O4/carbon foams composites with broadened bandwidth and excellent electromagnetic wave absorption performance. Compos. Part A **127**, 105627 (2019)

32. A. Feng et al., Fabrication of NiFe2O4@carbon fiber coated with phytic acid-doped polyaniline composite and its application as an electromagnetic wave absorber. RCS Adv. **9**, 25932–25941 (2019)

33. Z. Jia, Development of spindle-cone shaped of Fe/-Fe2O3 hybrids and their superior wideband electromagnetic absorption performance. J. Alloys Compd. **799**, 216–223 (2019)

34. F. Costa, A. Monorchio, Electromagnetic absorbers based on high-impedance surfaces: from ultra-narrowband to ultra-wideband absorption. Adv. Electromagn. **1**(3), 7–12 (2012)

35. F. Costa et al., Efficient analysis of frequency-selective surfaces by a simple equivalent-circuit model. Antennas Propag. Mag. IEEE **54**(4), 35–48 (2012)

36. X. Huang et al., Experimental demonstration of printed graphene nano-flakes enabled flexible and conformable wideband radar absorber. Sci. Rep. **6**, 38197 (2016)

37. W.J. Lee et al., Characteristics of an electromagnetic wave absorbing composite structure with a conducting polymer electromagnetic bandgap (EBG) in the X-band. Compos. Sci. Technol. **68**, 2485–2489 (2008)

38. Y. Gao et al., Inkjet printing patterns of highly conductive pristine graphene on flexible substrates. Ind. Eng. Chem. Res. **53**(43), 16777–16784 (2014)

39. O.-S. Kwon et al., Fabrication and characterization of inkjet-printed carbon nanotube electrode patterns on paper. Carbon **58**, 116–127 (2013)

40. H.Ki Kim et al., Flexible inkjet-printed metamaterial absorber for coating a cylindrical object. Opt. Express **23**(5), 5900 (2015)

41. A. Rathmell et al., The synthesis and coating of long, thin copper nanowires to make flexible, transparent conducting films on plastic substrates. Adv. Mat. **23**, 4798–4803 (2011)

42. R.P. Tortorich, J.-W. Choi, Inkjet printing of carbon nanotubesD. Nanomaterials **3**, 453–468 (2013)

43. K.-Y. Shin et al., Micropatterning of graphene sheets by inkjet printing and its wideband dipole-antenna application. Adv. Mater. **23**, 2113–2118 (2011)

AQ5

44. S.K. Eshkalaka et al., A review on inkjet printing of CNT composites for smart applications. Appl. Mater. Today **9**, 372–386 (2017)

45. J. Li et al., Efficient inkjet printing of graphene. Adv. Mater. **25**(29), 3985–3992 (2013)

46. E.B. Secor et al., Inkjet printing of high conductivity, flexible graphene patterns. J. Phys. Chem. Lett. **4**, 1347–1351 (2013)

47. W. Baaziz et al., Magnetic iron oxide nanoparticles: reproducible tuning of the size and nanosized-dependent composition, defects, and spin canting. J. Phys. Chem. C **118**, 3795–3810 (2014)

48. N. Quiévy et al., Electromagnetic absorption properties of carbon nanotube nanocomposite foam filling honeycomb waveguide structures. IEEE Electromag. Compat. **54**(1), 43–51 (2012)

49. I. Molenberg et al., Simple, convenient and non-destructive electromagnetic characterisation technique for composite and multiscale hybrid samples at microwave frequencies. Microw. Opt. Technol. Lett. **56**(2), 504–509 (2014)

50. D. Pozar, Microwave Engineering, 4th edn (2012)

51. Ra'di et al., Thin perfect absorbers for electromagnetic waves: Theory,

design, and realizations. Phys. Rev. Appl. **3**, 037001 (2015)

52. L. Li, Z. Lv, Ultra-wideband polarization-insensitive and wide-angle thin absorber based on resistive metasurfaces with three resonant modes. J. Appl. Phys. **122**, 055104 (2017)

AQ6

53. C. Wang et al., Radar stealth and mechanical properties of a broadband radar absorbing structure. Compos. Part B **123**, 19–27 (2017)

54. Y. Shang et al., On the design of single-layer circuit analog absorber using double-square-loop array. IEEE Trans. Antennas Propag. **61**, 6022–6029 (2013)

55. K.-Y. Shin et al., Micropatterning of graphene sheets by inkjet printing and its wideband dipole-antenna application. Adv. Mater. **23**, 2113–2118 (2011)